A Battery Made from a Single Material

Fudong Han, Tao Gao, Yujie Zhu, Karen J. Gaskell, and Chunsheng Wang*

All-solid-state lithium-ion batteries (ASSLIBs) are receiving intense interest for energy storage systems because the replacement of the volatile and flammable liquid electrolyte[1] with nonflammable inorganic solid electrolyte could essentially improve the safety and reliability of the battery.[2] The conventional ASSLIBs consist of three distinct components: an anode, an electrolyte, and a cathode. In addition, current collectors should also be used to ensure the electron transport through the electrodes and the external circuit. The anode, cathode, and electrolyte normally use three different materials due to the stringent different requirements for each component. The electrodes are expected to be reversibly lithiated/delithiated at a low potential (anode) or a high potential (cathode) with good mixed electronic/ionic conductivities, whereas the electrolyte should have a wide electrochemical stability window with a very high ionic conductivity but negligible electronic conductivity. To develop a highly performed ASSLIB, two critical challenges have to be overcome: one is the high ionic resistance of the solid electrolyte and the other is the large interfacial resistance between the solid electrodes and solid electrolyte. Because of the great success in minimizing the solid electrolyte thickness based on a series of advanced deposition techniques, thin-film ASSLIBs (total thickness ≈15 μm) using low-conductivity solid electrolyte (LIPON with $\sigma_{Li} \approx 10^{-6}$ S cm^{-1}) have received extensive research.[3,4] Despite excellent cycle stability, the limited stored energy and the expensive, multistep fabrication process of this thin-film battery are still the main obstacles toward their wide applications.

Increasing the thickness of the electrodes and electrolyte to make the so-called bulk-type ASSLIBs (**Figure 1**a) is highly desired for their widespread use in the large-scale energy storage systems.[5] However, the performances of this type of battery, especially in terms of power density and cycle life, are too low for their practical applications. This is because the increase in the thickness of the battery would require a high ionic conductivity of the solid electrolyte and a very low interfacial resistance between the electrodes and electrolyte. Considerable efforts have been focused on developing highly conductive materials as solid electrolytes.[6–9] Even though the solid electrolyte with a comparable or a higher ionic conductivity than the liquid electrolyte was used, and more solid electrolyte (≈50 wt%

compared with ≈30 vol% for liquid electrolyte LIBs) and a large amount of electronically conductive additive (25 wt% carbon for Li$_2$S) were added in the composite electrodes, the rate and cycling performances of the bulk-type ASSLIBs are still much lower than those of the liquid electrolyte LIBs with similar loading of the electrodes.[10] Bulk-type ASSLIBs using ductile sulfide electrolytes ($\sigma_{Li} > 10^{-3}$ S cm^{-1}) are only operated at very low current densities,[11–13] and the ones using rigid oxide electrolytes (e.g., garnet-type Li$_7$La$_3$Zr$_2$O$_{12}$ with $\sigma_{Li} > 10^{-4}$ S cm^{-1}) can hardly even be cycled because of the huge overpotentials during the charge/discharge process.[10] These results indicate that the interfacial resistance between the solid electrodes and solid electrolyte is becoming the dominant kinetic limitation, given the significantly decreased resistance of the electrolyte layer by using highly conductive solid electrolyte.[14]

The highly resistive interface was mainly resulted from the insufficient contact between solid electrodes and solid electrolyte because the solid electrolytes are not wettable and infiltrative like liquids. The poor interfacial contact restricts the fast transport of lithium ions and also decreases the number of active sites for charge transfer reaction. Various attempts have been made to improve the interfacial contact by reducing the electrode particle size,[15] uniaxial or dynamic pressing,[11,16] molten salt,[17,18] screen printing,[19] lattice matching,[20] and one-step spark plasma sintering methods.[21,22] However, only limited success in enhancing the power density has been achieved because a new interfacial phase layer with a high resistance might also be generated from the unwanted chemical reactions[23–25] and elemental interdiffusions[26] between the different electrode and electrolyte materials during either synthesis or the charge/discharge cycles. Even worse, the intimate initial contact achieved in the fabrication and/or sintering process may even accelerate the unwanted chemical reactions and elemental interdiffusions.[23,27] In addition, the space-charge layers formed at the heterointerface between the electrode and electrolyte due to their electrochemical potential difference might also increase the interfacial resistance.[28,29] To minimize these unwanted interfacial interactions (chemical reactions, elemental interdiffusions, and space-charge layer formations), intentional surface coatings with various materials, including ionically conductive,[28,30] electronically conductive,[31] or even insulating layers,[32] on the electrodes were also reported. Despite apparent improvements using the above-mentioned methods, the interfacial resistance still remains too high and may even continuously increase with charge/discharge cycles.[33] The continuous increase of the interfacial resistance with charge/discharge cycles could be mainly related to the high strain/stress generated at the interface because the large volume changes of the electrodes (especially for the high-capacity electrodes) during lithiation/delithiation are highly constrained by the solid electrolyte.[34] Unfortunately, this problem gets even worse for a thicker electrode that is desired for a high energy density battery.

F. Han, T. Gao, Dr. Y. Zhu, Prof. C. Wang
Department of Chemical and Biomolecular Engineering
University of Maryland
College Park, MD 20742, USA
E-mail: cswang@umd.edu
Dr. K. J. Gaskell
Department of Chemistry and Biochemistry
University of Maryland
College Park, MD 20742, USA
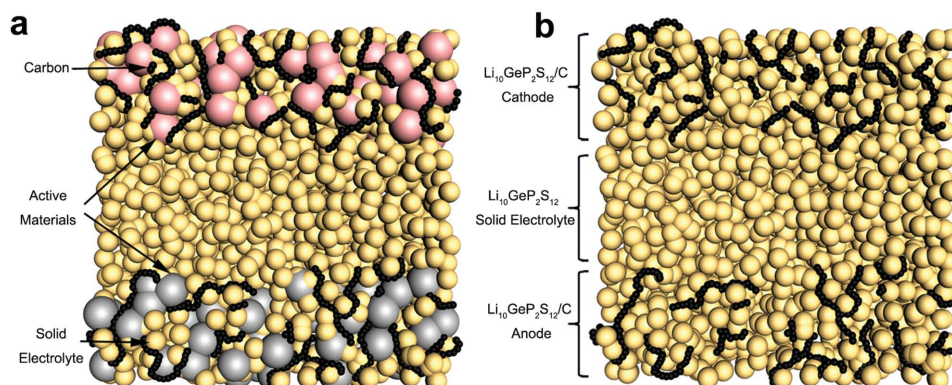
Figure 1. Schematic diagrams of a) a typical bulk-type all-solid-state lithium-ion battery and b) a single-$Li_{10}GeP_2S_{12}$ all-solid-state lithium-ion battery.

To overcome the intrinsic limitations of those aforementioned methods, a new concept of growing an electrode from an electrolyte[35,36] or growing an electrolyte from an electrode[37] has been reported to achieve intimate and stabilized interfacial contact in the ASSLIBs. For instance, a lithium metal anode could be in situ formed in the "Li-free" thin-film ASSLIBs by electrochemical plating during the initial charge,[35] and a MnO_2 cathode could also be in situ formed at the interface through the reaction between the $Li_{1+x+y}Al_yTi_{2-y}Si_xP_{3-x}O_{12}$ electrolyte (OHARA sheet) and Mn current collector under an external high driving force (16 V D.C. voltage).[36] Additionally, a solid electrolyte of LiI could also be in situ formed at the negative electrode/positive electrode interface through the chemical reaction of Li anode and I_2 cathode.[37] All of these in situ formed materials could facilitate the formation of a good electrode/electrolyte interface with a low resistance. However, the in situ formed electrode (or electrolyte) material is still different from the parent electrolyte (or electrode) material, thus the interface between electrode and electrolyte still exists and the strain/stress at the interface will be generated during lithiation/delithiation cycles. Ideally, the electrode and electrolyte should use the same material, in which case the interface between electrolyte and electrode will be eliminated or at least minimized to the level of internal electrode resistance (such as the internal interface resistance of a conversion electrode where the metal nanoparticles are uniformly distributed in the Li-ion conducting matrix). Although the well-known solid electrolytes, OHARA sheet and $Li_{3x}La_{2/3-x}TiO_3$ (LLTO), can also serve as anodes at a low potential due to the existence of Ti^{4+},[36,38–40] providing an ideal interface between the anode and electrolyte. Both OHARA and LLTO cannot serve as cathodes and therefore a different cathode material is still required for a battery, which would lead to a high resistive cathode/electrolyte interface. The Fe-doped LLTO (LLFTO) electrolyte has two lithiation/delithiation potential plateaus at 2.1 and 1.7 V, but the high electronic conductivity of LLFTO and low voltage between two plateaus (<0.4 V) limit its application only for an electrochromic device that has to be operated under a constant voltage due to high self-discharge rate.[40,41] To the best of our knowledge there is no any single material which could be used for all the electrolyte, anode, and cathode for high-energy Li-ion batteries.

Herein, we reported a novel high energy single-material ASSLIB (Figure 1b) to address the interfacial problem, wherein the cathode, electrolyte, and anode were made from a single material. The feasibility of using the highly conductive $Li_{10}GeP_2S_{12}$ (LGPS) electrolyte as both a cathode and an anode after mixing with electronically conductive carbon allows us to use it as a model material for the single-material ASSLIB. It would be expected that a perfect physical contact between the electrodes and electrolyte could be intrinsically achieved, the unwanted interfacial interactions could be avoided, and the strain/stress at the interface could be alleviated. As a result, a superior electrode/electrolyte interface with an extremely low resistance could be achieved in the single-LGPS ASSLIB, beneficial to a high-power, high-energy, and long-cycling all-solid-state battery with a low cost.

The realization of a single-material all-solid-state lithium-ion battery is based on the fact that some highly ionic conductive solid electrolytes could store Li ions at both a high and a low potential after incorporating electronic conductive materials. With the above considerations, $Li_{10}GeP_2S_{12}$ was used as a model material to demonstrate the single-material battery concept. LGPS has the highest ionic conductivity ($\sigma_{Li} \approx 10^{-2}$ S cm^{-1}) in all solid electrolytes.[7] The electrochemical window of LGPS was reported as high as ≈ 5.0 V.[7] Several >4.0 V ASSLIBs using LGPS as the solid electrolyte have also been fabricated.[42,43] However, the measured wide stability window of 5.0 V benefits from the poor kinetics of the oxidation and reduction reactions of LGPS due to its low electronic conductivity ($\sigma_e \approx 10^{-9}$ S cm^{-1}),[7] since the intrinsic thermodynamic stability window of LGPS is calculated to be only less than 2.5 V.[44] The theoretical calculation from first principle modeling also indicates that LGPS will be oxidized to P_2S_5, S, and GeS_2 at high potentials and be reduced to Li_2S, Li_3P, and $Li_{15}Ge_4$ at a low potential.[44] The S in the oxidation product of LGPS and the $Li_{15}Ge_4$ in the reduction product of LGPS are well-known cathode and anode materials, respectively, for a lithium-ion battery in a charged state if electronic conductive materials are introduced into two electrodes. Therefore, both the oxidative and reductive reactions could reversibly occur beyond the stability window of LGPS, and LGPS–carbon composite may be used as both a cathode and anode due to the enhanced reaction kinetics. Actually, the Li–S component in LGPS has the same local structure as Li_2S, which is a well-accepted cathode with a theoretical capacity of 1166 mAh g^{-1} at ≈ 2.2 V,[15,45] indicating that LGPS may probably function as a cathode after mixing with carbon.

In addition, it is known that the Sn–O component contained in $Sn_{1.0}B_{0.56}P_{0.40}Al_{0.42}O_{3.6}$ (TCO glass) is still electroactive for lithiation/delithiation as an anode even after a new phase formation.[46] Given the similarity between Sn—O in TCO and Ge—S in LGPS, LGPS may also function as an anode after mixing with carbon, since GeS_2 is a well-accepted anode with a theoretical capacity of 863 mAh g^{-1} at ≈0.5 V.[47,48] Thus, after mixing with carbon, LGPS could likely be able to serve as both a cathode and an anode. At a low potential the Ge–S component will be active for lithiation/delithiation but the Li–S component will remain inactive, and at a high potential only the Li–S component will be active. Therefore, pure LGPS could be used as the solid electrolyte while LGPS–carbon composites (LGPS/C) could serve as both a cathode and an anode. A single-LGPS ASSLIB could be fabricated by simply sandwiching LGPS/C cathode, LGPS solid electrolyte, and LGPS/C anode (Figure 1b), wherein carbon is considered as the extension of current collectors.

The feasibility of the single-LGPS ASSLIB has also been experimentally demonstrated. LGPS was synthesized following the previous report.[7] The Rietveld refinement of its X-ray powder diffraction pattern (**Figure 2**a) indicates that the as-obtained LGPS has a typical space group of $P4_2/nmc$ with the cell parameters of $a = 8.6995(3)$ Å, $c = 12.669(6)$ Å, and $V = 954.1$ Å^3, which is in good agreement with the previous report.[7] The green line in Figure 2a means the difference between experimental and calculated patterns. The fluctuation at low angles is due to experimental errors including the systematic errors and the structural deviations or minor impurities in the sample. The atomic ratio of P to Ge in the sample was determined to be 2.06 by inductively coupled plasma (ICP) spectroscopy (Figure S1, Supporting Information), consistent with the stoichiometric ratio of P/Ge = 2 in $Li_{10}GeP_2S_{12}$. The SEM image (Figure 2b) reveals that the particle size of the sample is about 2–5 μm. Figure 2c shows the Arrhenius plot of LGPS calculated from the impedance spectroscopy shown in the inset. Both the grain boundary and bulk conductivities are included. At 27 °C, the ionic conductivity of the cold-pressed LGPS is 7.4 mS cm^{-1}, which is lower than that of the previous annealed LGPS.[7] The reduced ionic conductivity may be due to the lower density of cold-pressed LGPS pellet. Additionally, the presence of minor impurities, as can be observed from the XRD pattern, may also contribute to the decrease of the ionic conductivity. The activation energy for the ionic transport was calculated to be 0.26 eV.

Figure 2d shows the electrochemical window of the LGPS obtained from cyclic voltammetry (CV) of a Li/LGPS/Pt cell at a scan rate of 0.05 mV s^{-1}. The LGPS is observed to be stable at a
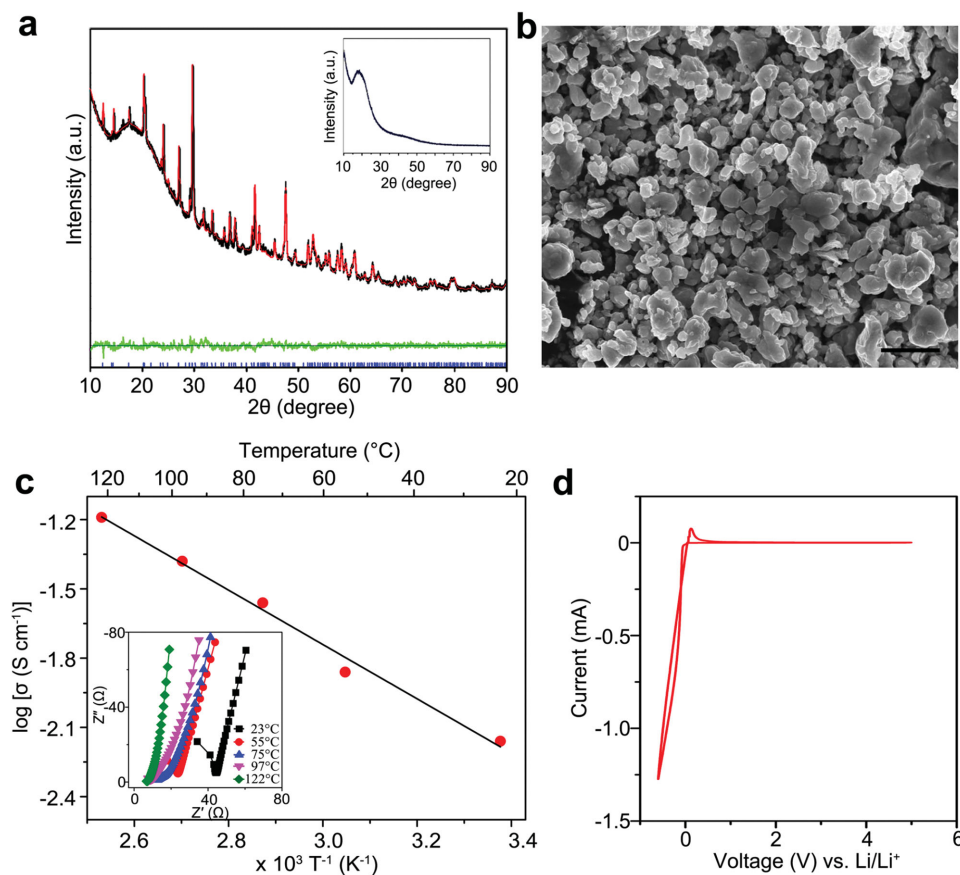
Figure 2. Characterizations of as-obtained $Li_{10}GeP_2S_{12}$. a) XRD pattern and Rietveld refinement of the as-obtained LGPS powder. The black, red, and green lines represent the experimental, calculated, and difference patterns, respectively. The blue markers correspond to the position of diffraction lines. The inset shows the background XRD pattern of the tape used for testing. b) SEM image of the as-prepared LGPS powder (Scale bar is 5 μm). c) Arrhenius conductivity plots of LGPS. The inset was electrochemical impedance spectroscopy measured with Au/LGPS/Au cell at different temperatures. d) Cyclic voltammetry curve of Li/LGPS/Pt cell within the voltage range of −0.6 to 5.0 V at a scan rate of 0.05 mV s^{-1}.

COMMUNICATION

high potential up to 5.0 V, which agrees well with the previous report.[7,43] However, when the Pt is replaced by an LGPS–C layer (LGPS:carbon is 75:25 in weight) to form a Li/LGPS/LGPS–C half-cell, a reversible redox peak at a low potential between 0.0–0.5 V can be observed if the LGPS–C is scanned between 0.0 and 2.0 V, and another reversible redox peak located at the high potential of 1.6–2.7 V can also be observed if the LGPS–C is scanned between 1.0 and 3.5 V (Figure S2, Supporting Information). This result demonstrates that an LGPS–C composite can serve as both a cathode at 1.6–2.7 V and an anode at 0.0–0.5 V. The lack of these peaks in the CV of the Li/LGPS/Pt cell (Figure 2d) is because the contact area between LGPS and electronically conductive Pt is very small, thus the reaction currents are too small to be observed in the CV scan. In fact, the electrochemical oxidation and reduction reactions of LGPS at the interface between the LGPS and Au in the Au/LGPS/Au blocking electrode beyond the stability window have been detected using the sensitive electrochemical impedance spectrum (EIS) (Figure S3, Supporting Information). The EIS of the fresh Au/LGPS/Au electrode shows a typical Nyquist plot of a solid electrolyte with a nearly vertical capacitive line for blocking electrodes. However, after a linear potential scan of the Au/LGPS/Au cell at a very low scan rate of 0.005 mV s^{-1} from 0.0 to 2.7 V, the Nyquist plot turns into a typical battery-like behavior with charge-transfer semicircles in the medium frequency and a near 45° slope diffusion line in the low frequency. This result demonstrates that even the Au/LGPS/Au blocking electrode may turn into a single-LGPS microbattery because the LGPS electrolyte would be oxidized and reduced as electrodes when it contacts with the electronically conductive Au.[36] These results indicate that it is feasible to fabricate an ASSLIB based on the single-material LGPS.

The electrochemical performances of LGPS–C electrodes (LGPS:carbon is 75:25 in weight) were first tested in a coin cell using the liquid electrolyte (1 M lithium bis(trifluoromethanesulfonyl)imide (LiTFSI) in tetraethylene glycol dimethyl ether (TEGDME) and n-methyl-(n-butyl) pyrrolidinium bis(trifluoromethanesulfonyl)imide (PYR$_{13}$TFSI)). The cathode performance of LGPS was evaluated in the potential

range between 1.0 and 3.5 V (vs Li/Li$^+$) and the anode performance was measured between 0.0 and 2.0 V. **Figure 3**a shows the initial three charge/discharge curves of the LGPS cathode between 1.0 and 3.5 V. A small voltage bump followed by a plateau at ≈2.8 V could be observed during the first charging while the subsequent discharge curve exhibits two plateaus at 2.5 and 2.1 V, giving a specific charge capacity of 186 mAh g$_{(LGPS)}^{-1}$ and a discharge capacity of 151 mAh g$_{(LGPS)}^{-1}$. The galvanostatic charge/discharge curves and CV scans (Figure S4a, Supporting Information) are very similar to the behavior of a Li$_2$S cathode in a liquid electrolyte.[45] The bump observed at only the first charge process represents the kinetic activation process, and two plateaus showing up at the discharge process could possibly be attributed to the reduction process from solid sulfur to liquid high-order polysulfides, and from liquid high-order polysulfides to solid Li$_2$S$_2$ or Li$_2$S, respectively.[49] This result indicates that the Li–S component in LGPS could be electroactive for the cathode performance, and the irreversible capacity of the LGPS cathode is probably due to the expected "shuttle" reaction of high-order lithium polysulfides as in Li–S batteries.[50]

Figure 3b displays the charge/discharge behavior of the LGPS anode in the first three cycles between 0.0 and 2.0 V (vs Li/Li$^+$). An irreversible sloped plateau at 0.9–0.5 V and a reversible plateau at ≈0.5 V could be observed in the first cycle, consistent with the CV scans (Figure S4b, Supporting Information). It should be noted that this behavior is very similar to the GeS$_2$ anode.[47,48] The irreversible plateau at 0.9–0.5 V is attributed to the irreversible conversion reaction from GeS$_2$ to Ge and Li$_2$S, giving a large irreversible capacity during the first cycle. The reversible plateau could mainly correspond to the alloying/dealloying of Li and Ge,[47] which contributes a lot to the reversible capacity of 205 mAh g$_{(LGPS)}^{-1}$ for the first cycle. This result demonstrates that the Ge–S component in LGPS could still act as the active center for lithiation/delithiation as an anode, although the carbon and the phosphorus in LGPS–C electrode may also slightly contribute to the capacity. Figure 3c shows the cycling stability of the LGPS cathode and anode in the liquid electrolyte coin cell. Despite that capacity decays could be observed for both LGPS cathode and anode
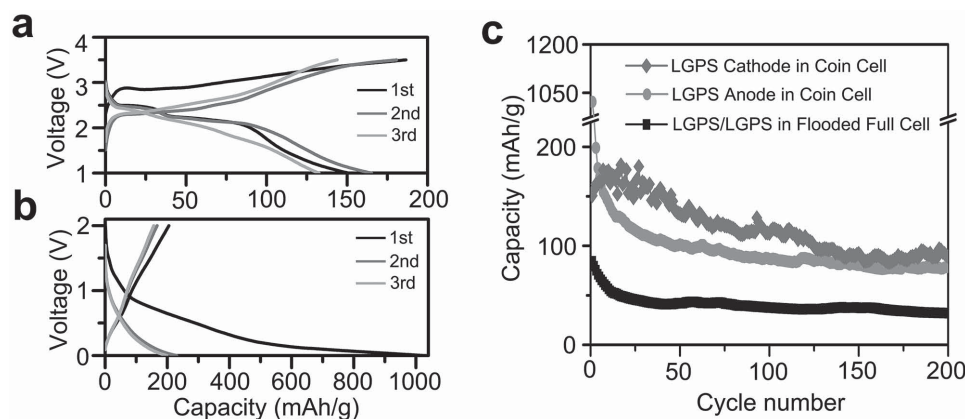
Figure 3. Electrochemical performance of Li$_{10}$GeP$_2$S$_{12}$ cathode and anode with liquid electrolyte. 1 M LiTFSI in TEGDME and PYR$_{13}$TFSI with a volume ratio of 1:1 was used as electrolyte for testing. Charge/discharge curves of Li/LGPS half-cell at a current density of 100 mA g$_{(LGPS)}^{-1}$ in the voltage range of a) 1.0–3.5 and b) 0.0–2.0 V. c) Cycling performance of the LGPS cathode, LGPS anode, and LGPS/LGPS flooded full cell. All the specific capacities are reported based on the weight of LGPS.

© 2015 WILEY-VCH Verlag GmbH & Co. KGaA, Weinheim
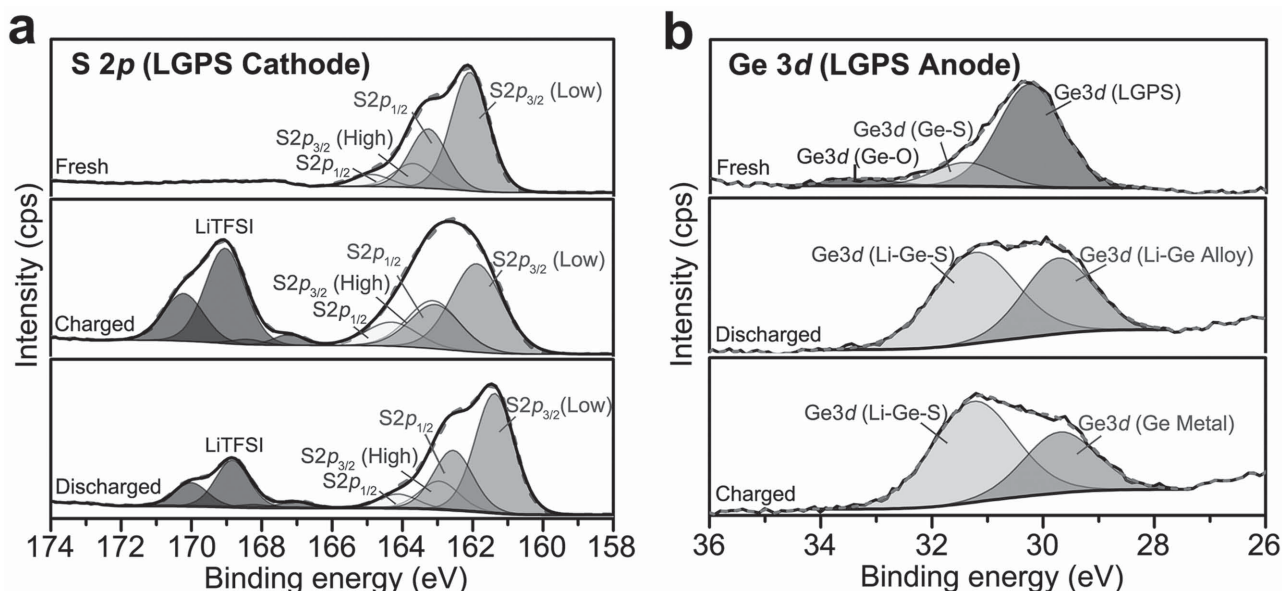
Figure 4. Deconvoluted S 2p and Ge 3d core XPS spectra of LGPS electrodes. a) S 2p spectrum of the LGPS cathode at the fresh state, charged to 3.5 V, and then redischarged to 1.0 V; b) Ge 3d spectrum of LGPS anode at the fresh state, discharged to 0.0 V, and then recharged to 2.0 V.

in the long-term charge/discharge cycles, the LGPS cathode and anode could still deliver 89 and 79 mAh $g_{(LGPS)}^{-1}$ after 200 cycles, respectively.

The cycling performance of the LGPS/liquid electrolyte/ LGPS full cell was tentatively examined in a three-electrode liquid electrolyte flooded cell using Li metal as a reference electrode (Figure 3c). The initial irreversible capacity of the LGPS anode was compensated by precycling the LGPS anode against Li reference electrode between 1.5 and 0 V. After the LGPS anode was recharged to 1.5 V, it was coupled with the fresh LGPS cathode to form an LGPS/liquid electrolyte/LGPS full cell. As shown in Figure 3c, the LGPS/LGPS full cell shows similar cycling stability as the individual LGPS anode and LGPS cathode thus demonstrating a high Coulombic efficiency of both the precycled LGPS anode and LGPS cathode during long-term charge/discharge cycles.

X-ray photoelectron spectroscopy (XPS) was used to understand the electrochemical reaction mechanisms of the LGPS cathode and anode in the liquid electrolyte. **Figure 4**a compares the XPS spectra of S 2p obtained from the LGPS cathodes at the fresh, fully charged (to 3.5 V) and fully discharged (to 1.0 V) states. The result indicates that all these cathodes exhibit a main peak around ≈163 eV, while the LGPS cathodes at fully charged and fully discharged states show another peak at ≈169 eV attributed to −SO$_2$CF$_3$ from the LiTFSI in the electrolyte.[51] The detailed fitting for the main peak of interest results in two peaks at ≈163.5 and ≈161.8 eV. Unfortunately, it is very difficult to designate either of them because of the complicated chemical environment of S in the samples (Ge–S, P–S, Li–S in LGPS, elemental sulfur, and a series of lithium sulfides), and therefore they were simply denoted as a high binding energy (B.E.) peak (at ≈163.5 eV) and a low B.E. peak (at ≈161.8 eV). Nevertheless, the electronegativity difference of cations that are bonded with S could tell a general trend of their binding energy positions (S–S > P–S > Ge–S > Li–S). Additionally, the peak for the bonding

with each cation will shift to a higher binding energy as the oxidation state of S increases, meaning that lithium sulfide with a sulfur oxidation state of −2 is always located in the low B.E. peak. These results allow us to use the area ratio of the low B.E. peak to the high B.E. peak to infer the reaction mechanism of the LGPS cathode (**Table 1**). The area ratio decreased from 4.9:1 for the fresh LGPS cathode to 1.8:1 after it was charged to 3.5 V indicating that the oxidation of sulfur (Li–S) to S–S occurred during the charge process. After the LGPS was discharged to 1.0 V, the ratio increased back to 4.2:1, which means the reduction of S. In addition, the area ratio after the first cycle (4.2:1) is very close to the original ratio for the fresh LGPS cathode (4.9:1), thus demonstrating the high reversibility of the reaction. This result confirmed that the cathode performance of LGPS could be attributed to the oxidation and reduction of the Li–S component contained within LGPS.

Figure 4b demonstrates the high resolution Ge 3d spectra of the LGPS anodes at the fresh, fully discharged (to 0.0 V) and fully charged (to 2.0 V) states. For the fresh LGPS anode, the main peak positioned at 30.3 eV could be attributed to the GeS$_4$ tetrahedra in the LGPS, while the other two small peaks at 31.3 and 33.3 eV stand for the Ge–S[52] and Ge–O[53] from the impurities or contaminants on the surface, respectively. However,

Table 1. XPS binding energies of low B.E. peak (E_{low}) and high B.E. peak (E_{high}) of S 2p spectra in LGPS cathodes.

| Samples	E_{low} S 2p$_{3/2}$ [eV]	E_{high} S 2p$_{1/2}$ [eV]	Area ratio
Fresh	162.1	163.7	4.9:1
Charged	161.9	164.3	1.8:1
Discharged	161.4	163.0	4.2:1

Note: The curve fits were obtained using fixed spin splits (2p$_{2/3}$ − 2p$_{1/2}$ = 1.18 eV) and fixed area ratio (2p$_{3/2}$/2p$_{1/2}$ = 2).

for the fully discharged and fully charged LGPS anodes, the main Ge 3d peak at 30.3 eV shifted to a high binding energy at 31.3 eV, while a new peak at 29.7 eV appeared. The new peak at 29.7 eV could be ascribed to the Ge metal.[54] Given the minimal difference of the binding energy between Ge-metal alloy[52] and Ge metal itself[54] due to the similar metallic bonding, the peak at 29.7 eV can also be ascribed to the Li–Ge alloy. The appearance of this peak confirms that the Ge–S component in LGPS is electroactive and would be reduced to a Li–Ge alloy after the first discharge to 0.0 V and oxidized back to the Ge metal after the LGPS anode was recharged to 2.0 V. The peak at 31.3 eV may be attributed to the Ge–S bonding in the residue intermediate product (Li–Ge–S compound) from an incomplete reaction of the LGPS anode. In addition, the high-resolution P 2p spectra of the LGPS anodes at the fresh, fully discharged, and fully charged states (Figure S5, Supporting Information) indicates that P contained in the LGPS has only a slight contribution to the reversible Li storage of the LGPS anode. Therefore, the anode performance of LGPS could mainly be attributed to the Ge–S component in LGPS, and it exhibits a similar reaction mechanism as the GeS_2 anode with an irreversible conversion reaction followed by a reversible alloying reaction.

Together with the charge/discharge behaviors of the LGPS cathode and anode discussed above, the XPS results confirm that the LGPS cathode and anode performance could be mainly attributed to the Li–S and Ge–S components in LGPS following the similar reaction mechanism as the Li_2S cathode and GeS_2 anode, respectively. Based on their stoichiometric ratio in LGPS, the theoretical capacities could be roughly calculated as 456 mAh $g_{(LGPS)}^{-1}$ for the LGPS cathode and 250 mAh $g_{(LGPS)}^{-1}$ for the LGPS anode (including the contribution from carbon black). This means that 41% and 80% of the theoretical capacity of the LGPS cathode and LGPS anode were achieved in the liquid electrolyte, respectively. The incomplete reactions are probably caused by the large particle size (2–5 μm) of LGPS electrodes and the nonuniform mixing of carbon through hand-grinding.
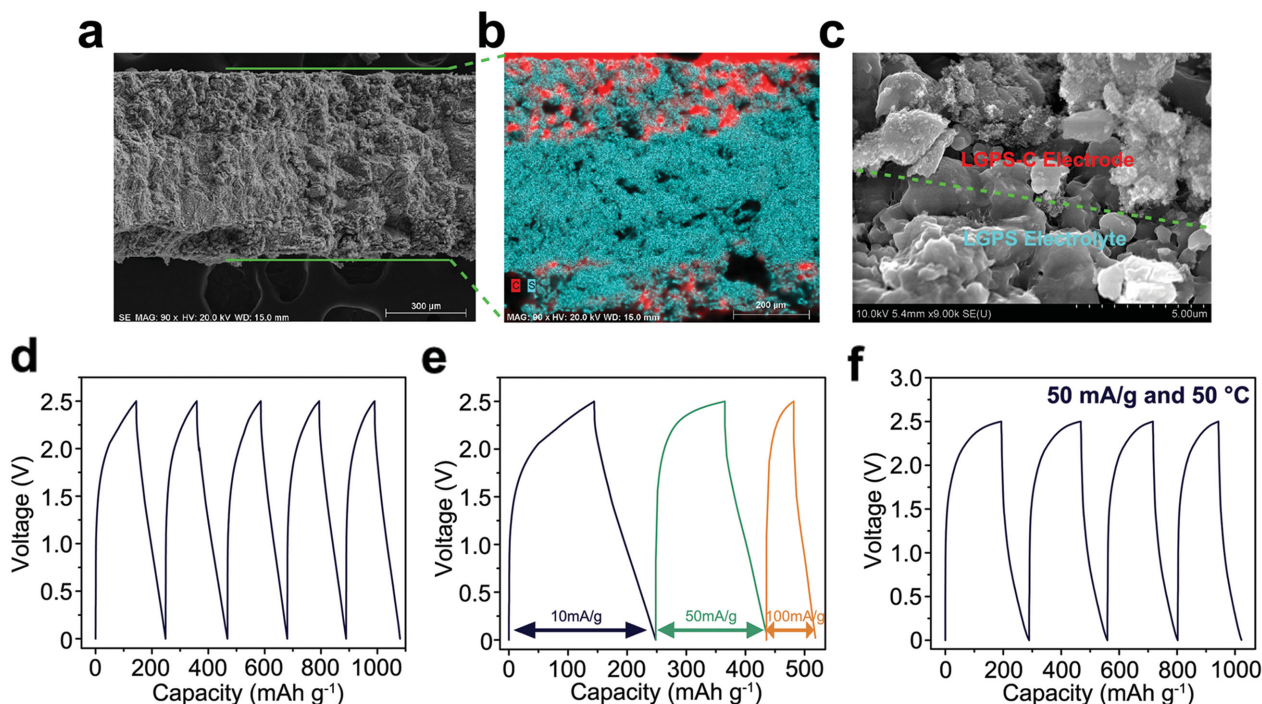
The electrochemical performances of all-solid-state batteries were tested in a specially designed Swagelok cell (**Figure 5**a), wherein the solid electrolyte and electrodes are cold-pressed sequentially between two stainless steel rods inside an insulating PTFE tank. The LGPS and carbon was ball-milled for 20 h to achieve a uniform distribution of the carbon in the composite electrode (Figure S6, Supporting Information). The half-cell tests (Li/LGPS/LGPS–C) within different voltage ranges were first conducted to evaluate the performances of the LGPS as a cathode and an anode in the all-solid-state configuration using LGPS as the solid electrolyte. Figure 5b shows that the LGPS cathode in the LGPS solid electrolyte exhibits a significantly different behavior from that measured in the liquid electrolyte (Figure 3a). No voltage bump corresponding to the activation process in the liquid electrolyte could be observed at the first charge process, and the subsequent discharge curve shows only one plateau at ≈2.2 V. The galvanostatic charge/discharge curves (Figure 5b) show one plateau in the charge/discharge curve. The one-plateau behavior of LGPS cathode in the solid-state battery may be attributed to the only binary solid–solid phase transition,[55] which is similar to the Li_2S electrodes in solid electrolyte.[15] The one redox couple in CV scans (Figure S2a, Supporting Information) of LGPS cathode also further confirms that the Li–S component contained in LGPS is mainly responsible for its cathode performance. The LGPS anode in the all-solid-state cell (Figure 5c) exhibits a very similar behavior as that in the liquid electrolyte (Figure 3b) with a large irreversible plateau at 0.9–0.5 V and a reversible plateau at ≈0.5 V in the first cycle, which is also consistent with the CV scans (Figure S2b, Supporting Information). An interesting phenomenon should be noted that a higher reversible capacity at the first cycle could be observed for both the LGPS cathode (275 mAh $g_{(LGPS)}^{-1}$) and anode (253 mAh $g_{(LGPS)}^{-1}$) in the all-solid-state half-cell than that in the liquid electrolyte cell. This is probably because of the activation of the LGPS solid electrolyte[15] and the much lower current density used in the all-solid-state battery test. In addition, the rate performances of the LGPS cathode and LGPS anode in the LGPS solid electrolyte at different current densities were also tested. As shown in Figure 5d, the LGPS cathode exhibits reversible capacities of 267, 140, 80 mAh $g_{(LGPS)}^{-1}$ at the current densities of 10, 50, 100 mA g^{-1}, respectively. Reversible capacities of 130, 60, and 36 mAh $g_{(LGPS)}^{-1}$ could be achieved for the LGPS anodes
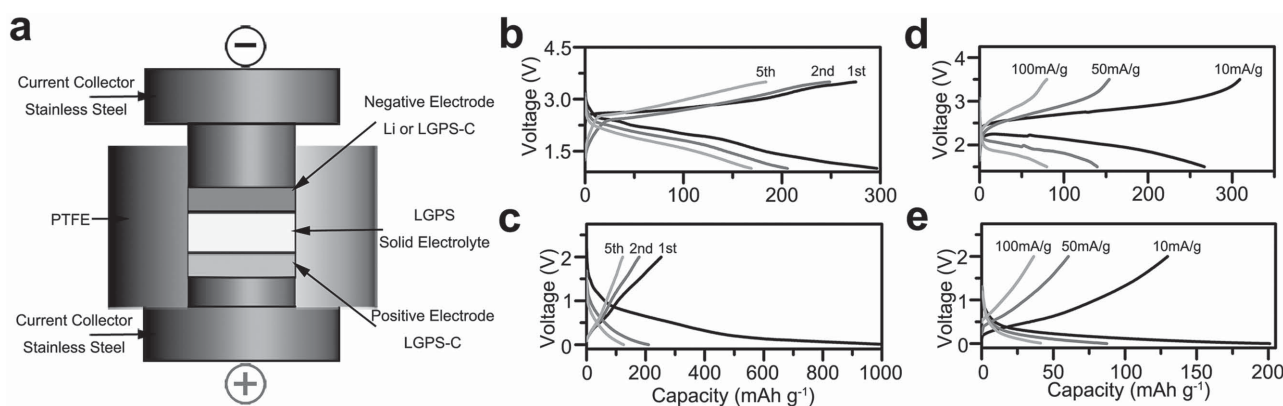
Figure 5. Electrochemical performance of $Li_{10}GeP_2S_{12}$ cathode and anode with $Li_{10}GeP_2S_{12}$ solid electrolyte. a) Schematic representation of the cell configuration for all-solid-state battery test. Charge/discharge curves of the Li/LGPS/LGPS–C all-solid-state cell at a current density of 10 mA g^{-1} in the voltage range of b) 1.5–3.5 and c) 0.0–2.0 V. d) Charge/discharge curve of the Li/LGPS/LGPS–C all-solid-state cell at different current densities in the voltage range of d) 1.5–3.5 and e) 0.0–2.0 V.

Figure 6. Electrochemical performance of the single-$Li_{10}GeP_2S_{12}$ battery. a) Cross-section SEM images of the single-LGPS battery. b) Elemental mappings of C (red) and S (blue) of the single-LGPS battery. c) High-magnification SEM image displaying the interface between LGPS electrode and LGPS electrolyte. d) Charge/discharge curves of the single-LGPS battery in the voltage range of 0.0–2.5 V from the second cycle at a current density of 10 mA g^{-1}. e) Charge/discharge curves of the single-LGPS battery in the voltage range of 0.0–2.5 V from the second cycle at different current densities. f) Charge/discharge curves of the single-LGPS battery in the voltage range of 0.0–2.5 V from the second cycle at 50 °C at a current density of 50 mA g^{-1}. The weight ratio of LGPS cathode to LGPS anode was tentatively set as 3 for the capacity balance. The specific capacity and the current density of the all-solid-state full cell were calculated based on the weight of LGPS anode. All the electrochemical performances of the batteries were tested at room temperature unless specified.

at the current densities of 10, 50, and 100 mA g^{-1}, respectively (Figure 5e).

The feasibility of using the Li superionic conductor LGPS electrolyte as both the cathode and anode allows us to build up a single-LGPS ASSLIB. To construct the single-LGPS all-solid-state full cell (LGPS–C/LGPS/LGPS–C), the weight ratio of the LGPS cathode to the LGPS anode was tentatively set as 3 to compensate the large irreversible capacity of the LGPS anode during the first discharge. **Figure 6**a shows the cross-section SEM image of the single-LGPS battery. No apparent delamination could be observed across the cell, indicating its great mechanical integrity. The layered composition of the cell identified from the elemental mapping was demonstrated in Figure 6b, from which we can see that the LGPS was continuously distributed across the entire thickness of the cell while the top and bottom layers of the LGPS were surrounded by carbon. The two different regions of the LGPS with and without carbon correspond to the LGPS electrodes and LGPS electrolyte, respectively, and the thicknesses of the cathode and anode are defined by the depth of carbon penetration. The thicknesses of the LGPS/C cathode, LGPS electrolyte, and LGPS/C anode layers in the single-LGPS battery are 222, 330, and 148 μm, respectively. The high-magnification image of the interface was also provided in Figure 6c. There is no clear distinction between the electrode and electrolyte except that some small

carbon black particles could be observed within the top layer of the LGPS. Figure 6d reveals the electrochemical behavior of the single-LGPS battery at a current density of 10 mA g^{-1} between 0.0 and 2.5 V, and it shows that the single-LGPS ASSLIB is able to deliver a reversible capacity of 104 mAh $g_{(LGPS)}^{-1}$. Moreover, similar charge/discharge curves could be observed from the second to the sixth cycle with no apparent capacity decay. The rate performance of the single-LGPS battery was also evaluated by cycling the battery at the current of 10, 50, and 100 mA g^{-1}, respectively. The result shown in Figure 6e indicates that the reversible capacity of the single-LGPS battery decreases from 104 to 37 mAh $g_{(LGPS)}^{-1}$ as the current increases from 10 to 100 mA g^{-1}. In addition, the electrochemical performance of the single-LGPS battery was also evaluated at an elevated temperature of 50 °C. As demonstrated in Figure 6f, at the current density of 50 mA g^{-1}, the reversible capacity of the single-LGPS battery increases from 70 to 96 mAh $g_{(LGPS)}^{-1}$ as the temperature increases from room temperature to 50 °C because of the decrease of the electrode, electrolyte, and interfacial resistances.

The interfacial behavior of the single-LGPS ASSLIB (LGPS–C/LGPS/LGPS–C) was evaluated by electrochemical impedance spectroscopy, and compared with a control battery (LGPS–C/80Li_2S·20P_2S_5/LGPS–C) which has exactly the same configuration, except with the replacement of LGPS with 80Li_2S·20P_2S_5 glass as the solid electrolyte. Both batteries were
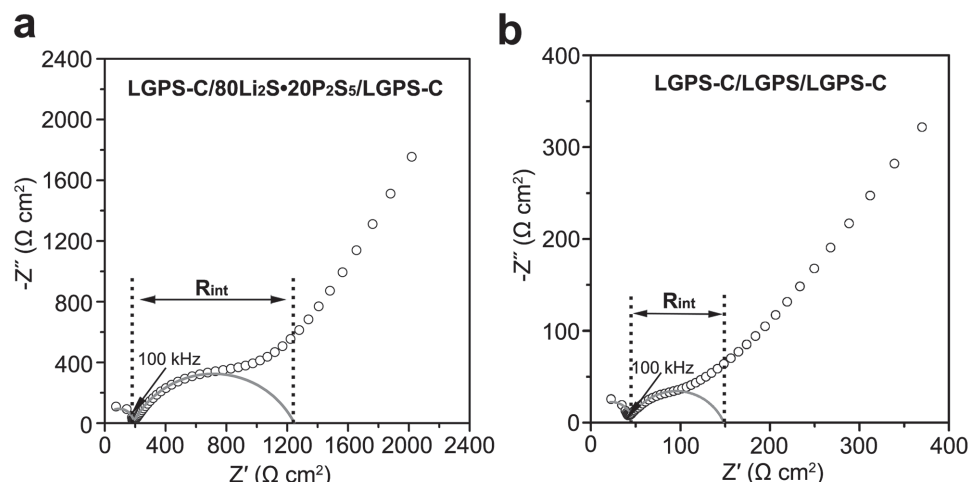
Figure 7. Impedance profiles of a) LGPS–C/80Li$_2$S·20P$_2$S$_5$/LGPS–C and b) LGPS–C/LGPS/LGPS–C all-solid-state LIBs after charging to 2.5 V in the 1–10^6 Hz frequency range at room temperature.

galvanostatically charged to 2.5 V, held at 2.5 V for 20 h, and rested at open-circuit potential for 2 h prior to EIS testing. **Figure 7** shows the EIS plots of these batteries at room temperature. Each EIS plot consists of a small semicircle in the high frequency region (>100 kHz) and a large semicircle in the medium frequency region, followed by a straight line corresponding to the Warburg impedance in the low frequency region. The small semicircle at high frequency could be assigned to the lithium ionic conduction in the solid electrolyte (R_{SE}) while the large semicircle corresponds to the interfacial resistance (R_{int}) between LGPS–C electrodes and solid electrolyte.[56] The resistance values were obtained by the least-square fittings of the impedance data using the equivalent circuit of two R//CPE (constant phase element) in series. As expected, the small difference in R_{SE} (192 Ω cm^2 for the LGPS/80Li$_2$S·20P$_2$S$_5$/LGPS cell and 45 Ω cm^2 for the LGPS/LGPS/LGPS cell) consists with the ionic conductivity difference of the solid electrolytes used. However, the interfacial resistance of the LGPS–C/80Li$_2$S·20P$_2$S$_5$/LGPS–C cell (1053 Ω cm^2) is about ten times higher than that of the single-LGPS battery (103 Ω cm^2), which might be the reason for the fast capacity decay of the LGPS–C/80Li$_2$S·20P$_2$S$_5$/LGPS–C cell (Figure S7, Supporting Information). Moreover, the area-specific interfacial resistance of the single-LGPS battery (103 Ω cm^2) is only 1.5 times of the electrodes in the liquid electrolyte battery (≈63 Ω cm^2),[57] although the single-LGPS battery has a 8–20 times higher loading of active material and ≈10 times larger thickness than that in the liquid electrolyte battery.[57] Despite the sensitivity of the EIS test to the processing of the battery (pressure used, relative content of the component in the composite electrode), the interfacial resistance of the single-LGPS battery is significantly lower than most of the bulk-type ASSLIBs.[10,21,32,58] Although the composition and fabrication process of single-LGPS battery have not been optimized, its interfacial resistance is still comparable to that of optimized ASSLIBs reported.[24,30] Since the ionic conductivity of solid electrolyte does not have significant influence on the interfacial resistance,[59] this result confirmed that the interfacial behavior could be remarkably improved in the single-material ASSLIB using the LGPS as both electrodes and electrolyte.

A single element arrangement (SEA) concept has been proposed by Weppner to prepare a fuel/electrolysis cell and an electrochromic cell using a single material.[60] Both of these devices exhibit low interfacial resistance by avoiding interfacial chemical reactions and mechanical disrupture. However, there is no report about using a single material for a rechargeable battery, wherein a severer compositional and structural change occurs at the electrode/electrolyte interface during charge/discharge. Herein, we reported the first single-material battery based on LGPS, which shows a remarkably improved interfacial performance as expected. The significant improvement of the interfacial behavior of the single-LGPS ASSLIB could be ascribed to the following reasons. i) Using a single LGPS as both the electrodes (cathode and anode) and the electrolyte would allow an intimate physical contact between the electrodes and electrolyte at an atomic scale since the electrodes are essentially evolved from the electrolyte. For a conventional bulk-type ASSLIB with poor electronically conductive electrodes, the charge transfer reaction usually occurs at the "triple phase contact" region where the active material should contact with both the lithium ionic conductive solid electrolyte and the electronically conductive carbon.[61] However, in the proposed single-LGPS ASSLIB, only a two-phase contact between carbon and solid electrolyte is required, which would effectively increase the active sites for electrochemical reaction. Since there is no carbon in the pure electrolyte layer and the electronic conductivity of LGPS cathode is very low, the progressive decomposition of the solid electrolyte would also be prevented. ii) The chemical reactions and elemental interdiffusion between electrodes and electrolyte could be eliminated because the electrodes are essentially gradually evolved from the electrolyte. More importantly, a transition region with a smooth chemical composition and potential gradient distribution could be formed across the electrodes and electrolyte.[62] The smooth electrochemical potential distribution will restrict the formation of space-charge layers between the electrodes and electrolyte. iii) The stress/strain generated at the interface would also be relieved because of the existence of the transition region across the electrodes and electrolyte. Consequently, a very low interfacial resistance could be achieved in

the single-LGPS ASSLIB during long-term charge/discharge cycles.

Despite the remarkable improvement of interface behavior, the electrochemical performance of the single-LGPS battery (Figure 5d,e) is still not as good as that in the liquid electrolyte battery (Figure 3a,b) at the same current density of 100 mA g^{-1}. This is because in the single-LGPS solid-state battery the loadings of LGPS in anode and cathode are 6 and 18 mg cm^{-2}, respectively, which are about 8–20 times higher than the LGPS loading in the liquid electrolyte cell (0.75 mg cm^{-2}). It is well known that the electrochemical performance of the electrode quickly decreases with the increase of the active material loading even in the liquid electrolyte battery. Moreover, the thickness of LGPS electrolyte layer (330 μm) used in the single-LGPS battery is about ten times larger than that of the separator (25–40 μm) used in the liquid electrolyte cell, which will also contribute to the high resistance of the battery. This could be supported by the fact that additional capacity of ≈20 mAh g$_{(LGPS)}^{-1}$ could be achieved at the current density of 10 mA g^{-1} by reducing the thickness of the LGPS electrolyte layer from 330 to 205 μm (Figures S8 and S9, Supporting Information). A series of engineering efforts are still required to further improve the performance of the proposed battery, such as the optimization of the content of carbon black in the composite electrodes, the design of porous, nanostructured electrodes, and the application of a constant pressure during testing. In particular, infiltration of electronic conductive materials into the porous layer of the porous LGPS/dense LGPS/porous LGPS sandwich structure using a mature technology in solid oxide fuel cell (SOFC) is more suitable for the single-material battery concept.[63] The key point of this work is to demonstrate a new single-material battery concept to address the interfacial problem for the bulk-type all-solid-state batteries. Moreover, the addition of large amounts of solid electrolyte (≈50 wt%) in the composite electrodes, which is usually required in a conventional bulk-type all-solid-state batteries (Figure 1a) to ensure efficient transport of lithium ions and electrons in the electrode volume, would be unnecessary for the single-material battery due to the high ionic conductivity of the electrode itself.

In summary, we demonstrated a proof of concept of a single-material battery using LGPS as the electrolyte, anode, and cathode, with the aim to eliminate the highly resistive interfacial resistance of ASSLIB. After mixing LGPS with carbon, the Li–S and Ge–S components in LGPS could act as active centers for its cathode and anode performance in a way similar to the Li$_2$S cathode and GeS$_2$ anode, respectively. The single-LGPS ASSLIB exhibited a remarkably low interfacial resistance due to: i) the improvement of interfacial contact, ii) the modification of the interfacial interactions, and iii) the suppression of the strain/stress at the interface. The single-material battery concept provides a promising direction to address the most challenging interfacial problem in all-solid-state lithium-ion battery. This concept is not limited to the use of LGPS, and it can also be broadly applied to other solid-state battery systems, beneficial to a high-power, high-energy, long-cycling all-solid-state battery. Additional implications of this concept include the fabrication of a nanobattery by introducing electronically conductive material on both the surfaces of the LGPS nanomaterials.

Experimental Section

Synthesis: Li$_{10}$GeP$_2$S$_{12}$ was prepared following a previous report.[7] Li$_2$S (Sigma–Aldrich, 99.98%), P$_2$S$_5$ (Sigma–Aldrich, 99%), and GeS$_2$ (MP Biomedicals LLC, 99.99%) were used as starting materials. These materials were weighed in the molar ratio of Li$_2$S/P$_2$S$_5$/GeS$_2$ = 5/1/1 in an argon (Ar)-filled glove box, subjected to a zirconia ceramic vial and mixed for 30 min using a high-energy vibrating mill (SPEX SamplePrep* 8000M Mixer/Mill). The powder obtained was then pressed into pellets, sealed in an evacuated quartz tube at 30 Pa, and heated at 550 °C for 8 h in a furnace placed inside the glove box. The sample was then naturally cooled down to the ambient temperature.

Characterization: Powder X-ray diffraction patterns were obtained with a D8 Advance with LynxEye and SolX (Bruker AXS, WI, USA) using Cu K$_\alpha$ radiation. The P/Ge ratio was determined by inductively coupled plasma spectroscopy (Perkin-Elmer ICP-OES). The morphology of the sample was examined using a Hitachi a SU-70 field-emission scanning electron microscope. The surface chemistry of the samples was examined by X-ray photoelectron spectroscopy using a Kratos Axis 165 spectrometer. To prepare the sample for XPS test, LGPS electrodes were charged or discharged to a certain voltage in a liquid electrolyte using a Swagelok cell, and held at that voltage for 24 h. The electrodes were then taken out from the cell, and rinsed by dimethoxyethane (DME) inside the glove box. All samples were dried under vacuum overnight, placed in a sealed bag, and then transferred into the XPS chamber under inert conditions in a nitrogen-filled glove bag. Ar$^+$ sputtering was performed for 180 s on the surface of the discharged and charged LGPS anodes to remove the SEI layer. XPS data were collected using a monochromated Al K$_\alpha$ X-ray source (1486.7 eV). The working pressure of the chamber was lower than 6.6 × 10^{-9} Pa. All reported binding energy values are calibrated to the C 1s peak at 284.8 eV.

Electrochemistry: The LGPS powder was pressed into a pellet (diameter 13 mm; thickness ≈2 mm) in an Ar atmosphere. It was then sputtered with Au to form an electrode for the ionic conductivity measurement. The electrochemical impedance spectrums of the Au/LGPS/Au cell were measured between 23 and 132 °C by applying a 100 mV amplitude AC potential in a frequency range of 10 MHz to 0.1 Hz. The cyclic voltammogram of the Li/LGPS/Pt cell was measured between −0.6 and 5.0 V with a scan rate of 0.05 mV s^{-1}. The electrochemical performances of LGPS electrodes were first tested using a liquid electrolyte with Celgard 3501 as the separator in either two- or three-electrode Swagelok cells. 1 M LiTFSI in a mixture of 1:1 volume ratio of TEGDME and PYR$_{13}$TFSI was used as the liquid electrolyte. Composite electrodes consisting of LGPS and carbon black with a weight ratio of 75:25 were prepared by hand-grinding in the mortar, which were then mixed with 10 wt% polyvinylidene fluoride (PVDF) and n-methylpyrrolidinone (NMP) to make the electrode slurries. The electrodes were prepared by casting these slurries onto stainless steel, copper, or aluminum foils and drying at 110 °C overnight inside the glove box. The loading of active material on each electrode is about 0.75 mg. Half-cells were assembled using a lithium metal foil as the counter electrode, and full cells in the liquid electrolyte were assembled with an electrode mass ratio of ≈1 between the cathode and the anode sides. For the assembly of the all-solid-state LGPS–C/LGPS/Li half-cell, the LGPS–C powder (10 mg) was put on the top of the LGPS powder (120 mg) and cold-pressed together under 360 MPa in a PTFE tank with a diameter of 13 mm. After that, a 100 μm thick lithium metal was then attached on the other side of the LGPS electrolyte layer as a counter and reference electrode. The formed three-layered pellet was then cold-pressed under 120 MPa between two stainless steel rods which serve as current collectors. The single-LGPS all-solid-state full cell was simply prepared by direct cold-pressing 10 mg LGPS–C powder as anode, 120 mg LGPS powder as solid electrolyte, and 30 mg LGPS–C powder as cathode under 360 MPa. Both the electrode preparation and cell assembly were performed in the Ar-filled glove box. The charge/discharge behavior was tested using an ArbinBT2000 workstation (Arbin Instruments, TX, USA) at room temperature. The electrochemical impedance spectrum and cyclic voltammetry measurements were carried on an electrochemistry workstation (Solartron 1287/1260).

COMMUNICATION

Supporting Information

Supporting Information is available from the Wiley Online Library or from the author.

[1] K. Xu, *Chem. Rev.* **2004**, *104*, 4303.

[2] T. H. Kim, J. S. Park, S. K. Chang, S. Choi, J. H. Ryu, H. K. Song, *Adv. Energy Mater.* **2012**, *2*, 860.

[3] J. B. Bates, N. J. Dudney, B. Neudecker, A. Ueda, C. D. Evans, *Solid State Ionics* **2000**, *135*, 33.

[4] V. P. Phan, B. Pecquenard, F. Le Cras, *Adv. Funct. Mater.* **2012**, *22*, 2580.

[5] P. H. L. Notten, F. Roozeboom, R. A. H. Niessen, L. Baggetto, *Adv. Mater.* **2007**, *19*, 4564.

[6] R. Murugan, V. Thangadurai, W. Weppner, *Angew. Chem. Int. Ed.* **2007**, *46*, 7778.

[7] N. Kamaya, K. Homma, Y. Yamakawa, M. Hirayama, R. Kanno, M. Yonemura, T. Kamiyama, Y. Kato, S. Hama, K. Kawamoto, A. Mitsui, *Nat. Mater.* **2011**, *10*, 682.

[8] Y. Seino, T. Ota, K. Takada, A. Hayashi, M. Tatsumisago, *Energy Environ. Sci.* **2014**, *7*, 627.

[9] F. Mizuno, A. Hayashi, K. Tadanaga, M. Tatsumisago, *Adv. Mater.* **2005**, *17*, 918.

[10] Y. Jin, P. J. McGinn, *J. Power Sources* **2013**, *239*, 326.

[11] M. Tatsumisago, F. Mizuno, A. Hayashi, *J. Power Sources* **2006**, *159*, 193.

[12] K. Takada, T. Inada, A. Kajiyama, M. Kouguchi, H. Sasaki, S. Kondo, Y. Michiue, S. Nakano, M. Tabuchi, M. Watanabe, *Solid State Ionics* **2004**, *172*, 25.

[13] T. A. Yersak, C. Stoldt, S. H. Lee, *J. Electrochem. Soc.* **2013**, *160*, A1009.

[14] K. Takada, *Langmuir* **2013**, *29*, 7538.

[15] M. Nagao, A. Hayashi, M. Tatsumisago, *J. Mater. Chem.* **2012**, *22*, 10015.

[16] M. J. G. Jak, M. S. Pontfoort, N. Van Landschoot, A. S. Best, E. M. Kelder, D. R. MacFarlane, M. Forsyth, J. Schoonman, *Solid State Ionics* **2001**, *143*, 57.

[17] P. Birke, F. Salam, S. Doring, W. Weppner, *Solid State Ionics* **1999**, *118*, 149.

[18] K. Chen, Y. Shen, Y. B. Zhang, Y. H. Lin, C. W. Nan, *J. Power Sources* **2014**, *249*, 306.

[19] S. Ohta, S. Komagata, J. Seki, T. Saeki, S. Morishita, T. Asaoka, *J. Power Sources* **2013**, *238*, 53.

[20] F. Rosciano, P. P. Pescarmona, K. Houthoofd, A. Persoons, P. Bottke, M. Wilkening, *Phys. Chem. Chem. Phys.* **2013**, *15*, 6107.

[21] A. Aboulaich, R. Bouchet, G. Delaizir, V. Seznec, L. Tortet, M. Morcrette, P. Rozier, J. M. Tarascon, V. Viallet, M. Dolle, *Adv. Energy Mater.* **2011**, *1*, 179.

[22] G. Delaizir, V. Viallet, A. Aboulaich, R. Bouchet, L. Tortet, V. Seznec, M. Morcrette, J. M. Tarascon, P. Rozier, M. Dolle, *Adv. Funct. Mater.* **2012**, *22*, 2140.

[23] K. H. Kim, Y. Iriyama, K. Yamamoto, S. Kumazaki, T. Asaka, K. Tanabe, C. A. J. Fisher, T. Hirayama, R. Murugan, Z. Ogumi, *J. Power Sources* **2011**, *196*, 764.

[24] T. Kobayashi, A. Yamada, R. Kanno, *Electrochim. Acta* **2008**, *53*, 5045.

[25] E. Jeong, H. A. Chan, Y. Tak, S. C. Nam, S. Cho, *J. Power Sources* **2006**, *159*, 223.

[26] A. Sakuda, A. Hayashi, M. Tatsumisago, *Chem. Mater.* **2009**, *22*, 949.

[27] R. Kanno, M. Murayama, T. Inada, T. Kobayashi, K. Sakamoto, N. Sonoyama, A. Yamada, S. Kondo, *Electrochem. Solid-State Lett.* **2004**, *7*, A455.

[28] N. Ohta, K. Takada, L. Q. Zhang, R. Z. Ma, M. Osada, T. Sasaki, *Adv. Mater.* **2006**, *18*, 2226.

[29] J. Haruyama, K. Sodeyama, L. Han, K. Takada, Y. Tateyama, *Chem. Mater.* **2014**, *26*, 4248.

[30] A. Sakuda, A. Hayashi, T. Ohtomo, S. Hama, M. Tatsumisago, *J. Power Sources* **2011**, *196*, 6735.

[31] R. B. Cervera, N. Suzuki, T. Ohnishi, M. Osada, K. Mitsuishi, T. Kambara, K. Takada, *Energy Environ. Sci.* **2014**, *7*, 662.

[32] J. H. Woo, J. E. Trevey, A. S. Cavanagh, Y. S. Choi, S. C. Kim, S. M. George, K. H. Oh, S. H. Lee, *J. Electrochem. Soc.* **2012**, *159*, A1120.

[33] S. Boulineau, J. M. Tarascon, J. B. Leriche, V. Viallet, *Solid State Ionics* **2013**, *242*, 45.

[34] T. Okumura, T. Nakatsutsumi, T. Ina, Y. Orikasa, H. Arai, T. Fukutsuka, Y. Iriyama, T. Uruga, H. Tanida, Y. Uchimoto, Z. Ogumi, *J. Mater. Chem.* **2011**, *21*, 10051.

[35] B. J. Neudecker, N. J. Dudney, J. B. Bates, *J. Electrochem. Soc.* **2000**, *147*, 517.

[36] C. Yada, Y. Iriyama, T. Abe, K. Kikuchi, Z. Ogumi, *Electrochem. Commun.* **2009**, *11*, 413.

[37] W. Greatbatch, J. H. Lee, W. Mathias, M. Eldridge, J. R. Moser, A. A. Schneider, *IEEE Trans. Biomed. Eng.* **1971**, *18*, 317.

[38] Y. Iriyama, C. Yada, T. Abe, Z. Ogumi, K. Kikuchi, *Electrochem. Commun.* **2006**, *8*, 1287.

[39] P. Birke, S. Scharner, R. A. Huggins, W. Weppner, *J. Electrochem. Soc.* **1997**, *144*, L167.

[40] M. Klingler, W. F. Chu, W. Weppner, *Ionics* **1997**, *3*, 289.

[41] W. Weppner, *Ionics* **2001**, *7*, 404.

[42] Y. Kato, K. Kawamoto, R. Kanno, M. Hirayama, *Electrochemistry* **2012**, *80*, 749.

[43] J. Hassoun, R. Verrelli, P. Reale, S. Panero, G. Mariotto, S. Greenbaum, B. Scrosati, *J. Power Sources* **2013**, *229*, 117.

[44] Y. F. Mo, S. P. Ong, G. Ceder, *Chem. Mater.* **2012**, *24*, 15.

[45] Y. Yang, G. Zheng, S. Misra, J. Nelson, M. F. Toney, Y. Cui, *J. Am. Chem. Soc.* **2012**, *134*, 15387.

[46] Y. Idota, T. Kubota, A. Matsufuji, Y. Maekawa, T. Miyasaka, *Science* **1997**, *276*, 1395.

[47] Y. Kim, H. Hwang, K. Lawler, S. W. Martin, J. Cho, *Electrochim. Acta* **2008**, *53*, 5058.

[48] Y. J. Cho, H. S. Im, Y. Myung, C. H. Kim, H. S. Kim, S. H. Back, Y. R. Lim, C. S. Jung, D. M. Jang, J. Park, E. H. Cha, S. H. Choo, M. S. Song, W. I. Cho, *Chem. Commun.* **2013**, *49*, 4661.

[49] S. S. Zhang, *J. Power Sources* **2013**, *231*, 153.

[50] Y. V. Mikhaylik, J. R. Akridge, *J. Electrochem. Soc.* **2004**, *151*, A1969.

[51] Y. S. Su, Y. Fu, T. Cochell, A. Manthiram, *Nat. Commun.* **2013**, *4*, 2985.

[52] G. Saffarini, J. Saiter, *Mater. Lett.* **2000**, *46*, 327.

[53] P. Timbrell, M. Puchert, R. Lamb, *Surf. Interface Anal.* **1994**, *21*, 731.

[54] K. Prabhakaran, T. Ogino, *Surf. Sci.* **1995**, *325*, 263.

[55] T. Takeuchi, H. Kageyama, K. Nakanishi, M. Tabuchi, H. Sakaebe, T. Ohta, H. Senoh, T. Sakai, K. Tatsumi, *J. Electrochem. Soc.* **2010**, *157*, A1196.

[56] Y. Noguchi, E. Kobayashi, L. S. Plashnitsa, S. Okada, J. Yamaki, *Electrochim. Acta* **2013**, *101*, 59.

[57] J. Li, C. Ma, M. Chi, C. Liang, N. J. Dudney, *Adv. Energy Mater.* **2015**, *5*, 1401408.

[58] K. Takada, N. Ohta, L. Q. Zhang, X. X. Xu, B. T. Hang, T. Ohnishi, M. Osada, T. Sasaki, *Solid State Ionics* **2012**, *225*, 594.

[59] T. Ohtomo, A. Hayashi, M. Tatsumisago, Y. Tsuchida, S. Hama, K. Kawamoto, *J. Power Sources* **2013**, *233*, 231.

[60] W. Weppner, *Ionics* **2003**, *9*, 444.

[61] N. Machida, H. Maeda, H. Peng, T. Shigematsu, *J. Electrochem. Soc.* **2002**, *149*, A688.

[62] K. Yamamoto, Y. Iriyama, T. Asaka, T. Hirayama, H. Fujita, K. Nonaka, K. Miyahara, Y. Sugita, Z. Ogumi, *Electrochem. Commun.* **2012**, *20*, 113.

[63] J. M. Vohs, R. J. Gorte, *Adv. Mater.* **2009**, *21*, 943.